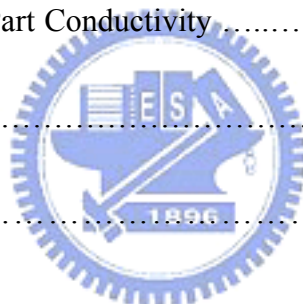


Contents

Chinese Abstract	i
English Abstract	v
Contents	xi
List of Figures	xiii
List of Tables	xxiii
Chapter 1 Introduction	1
Chapter 2 Experiments	15
2.1 Preparation and Characterization of Thin Films	15
2.1.1 Pulsed Laser Deposition System	16
2.1.2 Structure Characterization of Thin Films	17
2.1.2.1 X-ray Diffraction	18
2.1.2.2 Atomic Force Microscopy	19
2.1.3 Resistance (Resistivity) Measurement	20
2.2 Device Preparation	21
2.3 Oxygen-Controlling	22
2.3.1 Oxygen-Controlling Procedure	23
2.3.2 The Effects of Oxygen Stoichiometry on the Transport Properties of YBCO and Ca-YBCO Thin Films	26
2.4 Calibration and Microwave Measurements	28
Chapter 3 Theory	52
3.1 S Parameter	52
3.2 Losses of Microstrip Device	54
3.2.1 Conductor Loss	54
3.2.3 Dielectric Loss	57
3.2.2 Radiation Loss	59
3.3 Quality Factor (Q) of Resonator	59
3.3.1 Measured Quantities	59

3.3.2 Series Resonant Circuit	62
3.3.3 Total Losses of Resonator	65
3.3.4 Two Ports Measurements of Unloaded Quality Factor	68
3.4 Complex Conductivity	72
3.5 Penetration Depth	76
3.6 Some Models in Disordered d-wave Superconductors (Lee's model, Vishveshwara and Fisher's model)	84
Chapter 4 Results and Discussion	89
4.1 Determination of Hole Concentrations with Various Critical Temperatures	89
4.2 Resonance Frequency and Penetration Depth	90
4.2.1 Ferrel-Glover-Tinkham (FGT) Sum Rule	98
4.2.2 Fermi-Liquid Correction Factor	104
4.3 Quality Factor and Surface Impedance	108
4.3.1 Real Part Conductivity	111
4.3.2 Imaginary Part Conductivity	120
Chapter 5 Conclusion	182
References	185
Curriculum vitae	197

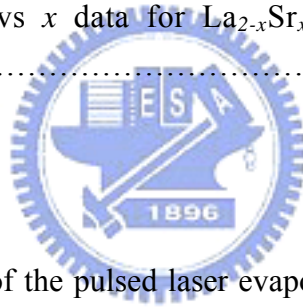


List of Figures

Chapter 1

Fig. 1.1. (a) Schematic phase diagram of HTSC which shows the evolution of various phases as a function of the in-plane hole concentration. (b) Schematic atomic structure of $\text{YBa}_2\text{Cu}_3\text{O}_{7-\delta}$. The dimensions of the unit cell are 3.82 \AA (a-axis) \times 3.89 \AA (b-axis) \times 11.68 \AA (c-axis) [12].13

Fig. 1.2. T_c , normalized to $T_{c,\text{max}}$, plotted as a function of hole concentration, p determined (i) from $p=x/2$ for $\text{Y}_{1-x}\text{Ca}_x\text{Ba}_2\text{Cu}_3\text{O}_6$ (solid squares), (ii) from $p=V_-$ for $\text{YBa}_2\text{Cu}_3\text{O}_{7-\delta}$ with different δ (open circles), (iii) from $p=V_-$ for $\text{Y}_{1-x}\text{Ca}_x\text{Ba}_2\text{Cu}_3\text{O}_{7-\delta}$ with $\delta \approx 0.04$ and different x (solid diamonds), and (iv) from $p=V_-$ for $\text{Y}_{1-x}\text{Ca}_x\text{Ba}_2\text{Cu}_3\text{O}_{7-\delta}$ with $x=0.1$ and different δ (crosses, \times). The solid curve is determined by $T_c/T_{c,\text{max}}=1-82.6(p-0.16)^2$, the “plus” symbols (+) are T_c vs x data for $\text{La}_{2-x}\text{Sr}_x\text{CuO}_4$ and solid triangles for $\text{La}_{2-x}\text{Sr}_x\text{CaCu}_2\text{O}_6$14



Chapter 2

Fig. 2.1. Schematic diagram of the pulsed laser evaporation system for deposition of thin films.34

Fig. 2.2. Ca L edge absorption spectra for $\text{Y}_{0.7}\text{Ca}_{0.3}\text{Ba}_2\text{Cu}_3\text{O}_{7-\delta}$ thin film. The two highest absorption peaks are due to the substitution of calcium to yttrium. The lower absorption peaks are due to the substitution of calcium to barium.35

Fig. 2.3. O K edge absorption spectra of XANES for $\text{Y}_{0.7}\text{Ca}_{0.3}\text{Ba}_2\text{Cu}_3\text{O}_{6.9}$ and $\text{YBa}_2\text{Cu}_3\text{O}_{6.9}$ thin films. The electric field of incident x-ray is perpendicular to c-axis.36

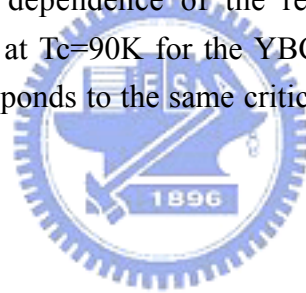
Fig. 2.4. The θ - 2θ X-Ray diffraction pattern for (a) $\text{YBa}_2\text{Cu}_3\text{O}_{7-\delta}$ and (b) $\text{Y}_{0.7}\text{Ca}_{0.3}\text{Ba}_2\text{Cu}_3\text{O}_{7-\delta}$ films, respectively.37

Fig. 2.5. The images of the surface morphologies of the YBCO thin film deposited on the LAO (100) substrate. (a). The surface roughness of the YBCO thin film

was 6.4 ± 2.7 nm. (b). The grain size of the YBCO thin film was 394 ± 115 nm.	38
Fig. 2.6. The images of the surface morphologies of the Ca-YBCO thin film deposited on the LAO (100) substrate. (a). The surface roughness of the YBCO thin film was 6.2 ± 3.4 nm. (b). The grain size of the Ca-YBCO thin film was 153 ± 24 nm.	39
Fig. 2.7. The temperature dependence of resistance for the $\text{YBa}_2\text{Cu}_3\text{O}_{7-\delta}$ and $\text{Y}_{0.7}\text{Ca}_{0.3}\text{Ba}_2\text{Cu}_3\text{O}_{7-\delta}$ thin films ($\delta \approx 0.05$), which shows that the zero resistance critical temperature $T_c \sim 91\text{K}$ for $\text{YBa}_2\text{Cu}_3\text{O}_{7-\delta}$ film and $T_c \sim 60\text{K}$ for $\text{Y}_{0.7}\text{Ca}_{0.3}\text{Ba}_2\text{Cu}_3\text{O}_{7-\delta}$ film, respectively. At $T=0\text{K}$, the extrapolated value of the resistance of $\text{Y}_{0.7}\text{Ca}_{0.3}\text{Ba}_2\text{Cu}_3\text{O}_{7-\delta}$ film is not equal to zero, and the reason maybe is due to lattice antisite disorder or defects after doping calcium impurities.	40
Fig. 2.8. The schematic diagram of the processes of patterning was described by the standard photolithography and wet etching method.	41
Fig. 2.9. The schematics of the ring-shaped microstrip resonator made of double-sided $\text{Y}_{0.7}\text{Ca}_{0.3}\text{Ba}_2\text{Cu}_3\text{O}_{7-\delta}$ thin films.	42
Fig. 2.10. The schematics of the microstrip line resonator made of double-sided $\text{Y}_{0.7}\text{Ca}_{0.3}\text{Ba}_2\text{Cu}_3\text{O}_{7-\delta}$ thin films.	43
Fig. 2.11. The oxygen pressure-temperature phase diagram of YBCO bulk.	44
Fig. 2.12. Transition temperature (T_c) vs oxygen content (δ) for thin-film samples of $\text{YBa}_2\text{Cu}_3\text{O}_{7-\delta}$ and polycrystalline $\text{YBa}_2\text{Cu}_3\text{O}_{7-\delta}$. For the thin-film samples the values of δ were measured using electron probe microanalysis (EPMA), and for the sintered samples from weight loss.	44
Fig. 2.13. The θ - 2θ X-Ray diffraction pattern for (a) $\text{YBa}_2\text{Cu}_3\text{O}_{7-\delta}$ with $\delta = 0.1$ and 0.25 (b) $\text{Y}_{0.7}\text{Ca}_{0.3}\text{Ba}_2\text{Cu}_3\text{O}_{7-\delta}$ with $\delta = 0.1$ and 0.25 , respectively.	45
Fig. 2.14. The temperature dependence of resistance for the $\text{YBa}_2\text{Cu}_3\text{O}_{7-\delta}$ thin films with various oxygen contents at $\delta = 0.05, 0.12, 0.15, 0.24, 0.26$ and 0.5 , respectively.	46

- Fig. 2.15. The temperature dependence of resistance for the $\text{YBa}_2\text{Cu}_3\text{O}_{7-\delta}$ thin films with various oxygen contents. Note that the resistance are measured form various YBCO samples.47
- Fig. 2.16. $\rho_{ab}(T)$ for a YBCO film with various oxygen contents. Curves 1 to 8 represent $7-\delta (=x) = 7.0, 6.9, 6.8, 6.75, 6.7, 6.55, 6.5,$ and $6.45,$ respectively. The inset shows the T_{c0} as a function of x48
- Fig. 2.17. The temperature dependence of d.c. resistivity for the $\text{Y}_{0.7}\text{Ca}_{0.3}\text{Ba}_2\text{Cu}_3\text{O}_{7-\delta}$ thin film with various oxygen contents.49
- Fig. 2.18. The photography is a HP8510 C Network Analyzer to measure the scattering parameters of a one- or two-port microwave network from 40 MHz to 20 GHz.50
- Fig. 2.19. The temperature dependence of the resonance frequency $f(T)$ and scattering matrix S_{21} at $T_c=90\text{K}$ for the YBCO film. The abrupt change for $f(T)$ and S_{21} corresponds to the same critical temperature.51

Chapter 3



- Fig. 3.1. (a) A series RLC circuit. (b) Equivalent circuit of a cavity resonator for two-port measurements.88

Chapter 4

- Fig. 4.1. The hole concentrations of the $\text{YBa}_2\text{Cu}_3\text{O}_{7-\delta}$ and the $\text{Y}_{0.7}\text{Ca}_{0.3}\text{Ba}_2\text{Cu}_3\text{O}_{7-\delta}$ thin films are obtained by using the empirical relation $T_c/T_{c,\text{max}}=1-82.6(p-0.16)^2$. Here $T_{c,\text{max}}$ for $\text{YBa}_2\text{Cu}_3\text{O}_{7-\delta}$ thin film is taken as 91K and the one for $\text{Y}_{0.7}\text{Ca}_{0.3}\text{Ba}_2\text{Cu}_3\text{O}_{7-\delta}$ thin film is taken as 84K.126
- Fig. 4.2. The temperature dependence of resonance frequency $f(T)$ of the ring resonator for the YBCO thin film with various hole concentrations p127
- Fig. 4.3. The temperature dependence of resonance frequency $f(T)$ of the ring resonator for the Ca-YBCO thin film with various hole concentrations p128

- Fig. 4.4. The temperature dependence of resonance frequency $f(T)$ of the microstrip line resonator for the YBCO thin film with various hole concentrations p . ..129
- Fig. 4.5. The temperature dependence of resonance frequency $f(T)$ of the microstrip line resonator for the Ca-YBCO thin film with various hole concentrations p130
- Fig. 4.6. The normalized temperature dependence of the change of resonance frequency $-\Delta f(T)/f(5K)=1-f(T)/f(5K)$ for the YBCO ring resonators with various hole concentrations p131
- Fig. 4.7. The normalized temperature dependence of the change of resonance frequency $-\Delta f(T)/f(5K)=1-f(T)/f(5K)$ for the Ca-YBCO ring resonators with various hole concentrations p132
- Fig. 4.8. The normalized temperature dependence of the change of resonance frequency $-\Delta f(T)/f(5K)=1-f(T)/f(5K)$ of the microstrip line resonator for the YBCO film with various hole concentrations p133
- Fig. 4.9. The normalized temperature dependence of the change of resonance frequency $-\Delta f(T)/f(5K)=1-f(T)/f(5K)$ of the microstrip line resonator for the Ca-YBCO film with various hole concentrations p134
- Fig. 4.10. The normalized temperature dependence of the resonance frequency $f(T)/f(5K)$ for the YBCO ring resonators with (a) $p=0.16$ and (b) $p=0.09$, respectively.135
- Fig. 4.11. The normalized temperature dependence of the resonance frequency $f(T)/f(5K)$ for the Ca-YBCO ring resonator with (a) $p= 0.218$ and (b) $p= 0.111$, respectively.136
- Fig. 4.12. The normalized temperature dependence of the resonance frequency $f(T)/f(5K)$ of the microstrip line resonators for (a) the YBCO thin film with $p =0.148$ and (b) the Ca-YBCO thin film with $p = 0.217$, respectively.137
- Fig. 4.13. Doping dependence of the a-b plane penetration depth $\lambda(5K)$. By using the Uemura relation, $n_s \propto T_c$, and the empirical formula $T_c/T_{c,max}=1-82.6(p-0.16)^2$,

one can obtain the doping dependence of $T_c(p)$. The dashed line is represented as $\lambda(p) = 200 \times (1 - 82.6(p - 0.16)^2)^{-0.5}$. The dotted line is represented as $\lambda(p) = 145 \times (1 - 82.6(p - 0.16)^2)^{-0.5}$138

Fig. 4.14. The normalized temperature dependence of the change of the penetration depth $\Delta\lambda$ for the (a) YBCO and (b) Ca-YBCO microstrip ring resonators with various hole concentrations p139

Fig. 4.15. The normalized temperature dependence of the change of the penetration depth $\Delta\lambda$ for the YBCO ring resonator with (a) $p = 0.148$ and (b) $p = 0.098$, respectively.140

Fig. 4.16. The normalized temperature dependence of the change of the penetration depth $\Delta\lambda$ for the Ca-YBCO ring resonator with (a) $p = 0.218$ and (b) $p = 0.088$, respectively.141

Fig. 4.17. The doping dependence of the $2\Delta_0/k_B T_c$ obtained from the BCS d-wave model for the YBCO and Ca-YBCO films. The average value (solid line) and the error bar of the all experimental data, $2\Delta_0/k_B T_c$ is 5.4 and 0.7, respectively.142

Fig. 4.18. The $1/\lambda^2(5K)$ vs p for the $Y_{0.7}Ca_{0.3}Ba_2Cu_3O_{7-\delta}$ and the $YBa_2Cu_3O_{7-\delta}$ thin films. Obviously, in the underdoped regime, it increases as increasing p . However, in the overdoped regime, it decreases as increasing p143

Fig. 4.19. The $T_c/T_{c,max}$ vs $1/\lambda^2(5K)$ for the $Y_{0.7}Ca_{0.3}Ba_2Cu_3O_{7-\delta}$ and the $YBa_2Cu_3O_{7-\delta}$ thin films. The dotted line shows the Uemura relation, $T_c \propto 1/\lambda^2(5K)$144

Fig. 4.20. Plot of superfluid density ($1/\lambda^2(5K)$) versus the product of the d.c. conductivity (σ_{dc}) and the superconducting transition temperature (T_c) for the YBCO and Ca-YBCO thin films with various oxygen contents. (σ_{dc} is measured just above the transition, and parallel to the CuO_2 (a-b) plane; data are shown on a linear scale) The values for σ_{dc} and $1/\lambda^2(5K)$ are obtained from standard four probe technique and microwave measurement, respectively. The $1/\lambda^2(5K)$ used in this scaling relation has been derived from the

in-plane London penetration depth $\lambda(5K)$ measurement, where $1/\lambda^2(5K)$ is proportional to the number of carriers in the condensate. The dotted, solid and dashed lines are described by $\lambda^{-2} = 4700\sigma_{dc}T_c$, $\lambda^{-2} = 5700\sigma_{dc}T_c$ and $\lambda^{-2} = 7500\sigma_{dc}T_c$, respectively.145

Fig. 4.21. The doping dependence of the normalized energy gap $2\Delta_0/k_B T_c$ for the YBCO and Ca-YBCO thin films. The ratio $2\Delta_0/k_B T_c$ appeared to be monotonic with the doping level p and it increased with decreasing doping. Inset: The doping dependence of the magnitude of energy gap Δ_0 for the YBCO and Ca-YBCO thin films.146

Fig. 4.22. The temperature dependence of $1/\lambda^2(T)$ with various hole concentrations for the (a) YBCO and (b) Ca-YBCO ring resonators at $T < 0.35T_c$147

Fig. 4.23. The doping dependence of Fermi liquid correction factor α for the YBCO and Ca-YBCO films.148

Fig. 4.24. The temperature dependence of the unloaded quality factor, Q , of the same YBCO ring resonator for $p = 0.16, 0.148, 0.134, 0.098, 0.09,$ and 0.074 , respectively.149

Fig. 4.25. The temperature dependence of the unloaded quality factor, Q , of the same Ca-YBCO ring resonator for $p = 0.218, 0.207, 0.188, 0.121, 0.111,$ and 0.088 , respectively.150

Fig. 4.26. The temperature dependence of the unloaded quality factor, Q , of the same YBCO microstrip line resonator for $p = 0.148, 0.106,$ and 0.09 , respectively.151

Fig. 4.27. The temperature dependence of the unloaded quality factor, Q , of the same Ca-YBCO microstrip line resonator for $p = 0.217, 0.197, 0.103, 0.092, 0.082,$ and 0.078 , respectively.152

Fig. 4.28. The temperature dependence of (a) the R_s and (b) the X_s of the YBCO ring resonator with $p = 0.16, 0.148, 0.134, 0.098, 0.09,$ and 0.074 , respectively.153

- Fig. 4.29. The temperature dependence of (a) the Rs and (b) the Xs of the Ca-YBCO ring resonator with $p = 0.218, 0.207, 0.188, 0.121, 0.111,$ and $0.088,$ respectively.154
- Fig. 4.30. The temperature dependence of (a) the Rs and (b) the Xs of the YBCO microstrip line resonator with $p = 0.148, 0.106,$ and $0.09,$ respectively.155
- Fig. 4.31. The temperature dependence of (a) the Rs and (b) the Xs of the Ca-YBCO microstrip line resonator with $p = 0.217, 0.197, 0.103, 0.092, 0.082,$ and $0.078,$ respectively.156
- Fig. 4.32. The temperature dependence of the real-part conductivity, $\sigma_1,$ of the (a) YBCO and (b) Ca-YBCO ring resonators with various hole concentrations.157
- Fig. 4.33. The normalized conductivity $\sigma_1/\sigma_1(5K)$ versus T_c/T for the YBCO and Ca-YBCO ring resonators with various hole concentrations.158
- Fig. 4.34. (a) The normalized conductivity $\sigma_1/\sigma_1(5K)$ versus T_c/T for the YBCO ring resonator with $p=0.1699$. The solid line is the formula, $\sigma_1/\sigma_1(5K) = (1 - Ae^{-c_1 T_c/T})$, fitted to the experimental data. (b) The normalized conductivity $\sigma_1/\sigma_1(5K)$ versus T_c/T for the YBCO ring resonator with $p=0.098$. The solid line is the formula, $\sigma_1/\sigma_1(5K) = (1 - Ae^{-c_1 T_c/T})$, fitted to the experimental data.159
- Fig. 4.35. (a) The normalized conductivity $\sigma_1/\sigma_1(5K)$ versus T_c/T for the Ca-YBCO ring resonator with $p=0.218$. The solid line is the formula, $\sigma_1/\sigma_1(5K) = (1 - Ae^{-c_1 T_c/T})$, fitted to the experimental data. (b) The normalized conductivity $\sigma_1/\sigma_1(5K)$ versus T_c/T for the Ca-YBCO ring resonator with $p=0.121$. The solid line is the formula, $\sigma_1/\sigma_1(5K) = (1 - Ae^{-c_1 T_c/T})$, fitted to the experimental data.160
- Fig. 4.36. The doping dependence of the characteristic energy scale, $T_{\sigma_1}^*, E_{g1}(0)$ and T_c was obtained from the numerical fitting of $\sigma_1/\sigma_1(5K)$ for the YBCO and Ca-YBCO ring resonators.161

- Fig. 4.37. The doping dependence of the vertex correction factor β . The dashed line is the average value of the experimental data and is 1.0 with the error bar of 0.5.162
- Fig. 4.38. The normalized temperature dependence of the scattering rate, $1/\tau$, of the (a) YBCO and (b) Ca-YBCO ring resonators with various hole concentrations. Obviously, the scattering rate approaches to a constant value at $T < 0.4T_c$163
- Fig. 4.39. The doping dependence of the energy scale Δ_0 , $T_{\sigma_1}^*$, $E_{g1}(0)$, γ_0 , $\hbar\frac{1}{\tau}$, ΔW , and T_c for the YBCO and Ca-YBCO thin films.164
- Fig. 4.40. The temperature dependence of the real-part conductivity, σ_1 , of the YBCO microstrip line resonator with $p = 0.148$, 0.106 and 0.09, respectively.165
- Fig. 4.41. The temperature dependence of the real-part conductivity, σ_1 , of the YBCO microstrip line resonator with $p = 0.148$. The broad peak was observed at $T \approx 35K$. The solid line is the fitting result of σ_1 at $T < 60K$ with the formula, $\sigma_1 = \sigma_1(5K)[(1 - Ae^{-c_1 T_c/T}) + a' \frac{T}{T_c}]$166
- Fig. 4.42. The temperature dependence of the real-part conductivity, σ_1 , of the YBCO microstrip line resonator with (a) $p = 0.106$ and (b) $p = 0.09$. The solid line is the fitting result of σ_1 with the formula, $\sigma_1 = \sigma_1(5K)(1 - Ae^{-c_1 T_c/T})$167
- Fig. 4.43. The temperature dependence of the real-part conductivity, σ_1 , of the Ca-YBCO microstrip line resonator with $p = 0.217$, 0.197, 0.103, 0.092, 0.082 and 0.078, respectively.168
- Fig. 4.44. The temperature dependence of the real-part conductivity, σ_1 , of the Ca-YBCO microstrip line resonator with $p = 0.217$, 0.197, 0.103, 0.092, 0.082 and 0.078, respectively. (a)-(c) The solid line is the fitting result of σ_1 with the formula, $\sigma_1 = \sigma_1(5K)[(1 - Ae^{-c_1 T_c/T}) + a' \frac{T}{T_c}]$. (d)-(f) The solid line is the fitting result of σ_1 with the formula, $\sigma_1 = \sigma_1(5K)(1 - Ae^{-c_1 T_c/T})$169

- Fig. 4.45. The doping dependence of the thermal activation gap, $E_{g1}(0)$, of the YBCO and Ca-YBCO thin films extracted from the microwave conductivity, $\sigma_1(T)$, measurements.170
- Fig. 4.46. The temperature dependence of the microwave real part conductivity, σ_1 , of YBCO single crystal extracted from the $R_s(T)$ and $X_s(T)$ measurements [76]. The solid line is the fitting result of σ_1 with the formula, $\sigma_1 = \sigma_1(5K)[(1 - Ae^{-c_1 T_c/T}) + a' \frac{T}{T_c}]$ at $T < 50$ K.171
- Fig. 4.47. The temperature dependence of the imaginary part of the microwave conductivity, σ_2 , for (a) the YBCO and (b) the Ca-YBCO ring resonators with various hole concentrations. The values of σ_2 increases as decreasing T at $T < T_c$ for all doping levels.172
- Fig. 4.48. Plot of $\sigma_2 / \sigma_2(5K)$ versus T_c/T for the YBCO and Ca-YBCO ring resonators with various hole concentrations.173
- Fig. 4.49. (a)-(b) Plot of $\sigma_2 / \sigma_2(5K)$ versus T_c/T for the YBCO ring resonator with (a) $p=0.16$ and (b) $p=0.098$, respectively. The solid line is the fitting result with the formula, $\sigma_2 / \sigma_2(5K) = (1 - Be^{-c_2 T_c/T})$. (c)-(d) Plot of $\sigma_2 / \sigma_2(5K)$ versus T_c/T for the Ca-YBCO ring resonator with (c) $p=0.218$ and (d) $p=0.121$, respectively. The solid line is the fitting result with the formula, $\sigma_2 / \sigma_2(5K) = (1 - Be^{-c_2 T_c/T})$174
- Fig. 4.50. The doping dependence of the characteristic energy scale, $T_{\sigma_2}^*$, $E_{g2}(0)$ and T_c of the YBCO and Ca-YBCO thin films was obtained from the fitting of $\sigma_2 / \sigma_2(5K)$175
- Fig. 4.51. The temperature dependence of the imaginary part of the microwave conductivity, σ_2 , for (a) the YBCO and (b) the Ca-YBCO microstrip line resonators with various hole concentrations. The values of σ_2 increases as decreasing T at $T < T_c$ for all doping levels.176
- Fig. 4.52. Plot of $\sigma_2 / \sigma_2(5K)$ versus T_c/T for the YBCO and Ca-YBCO microstrip

line resonators with various hole concentrations.177

Fig. 4.53. (a)-(b) Plot of $\sigma_2/\sigma_2(5K)$ versus T_c/T for the YBCO microstrip line resonator with (a) $p=0.148$ and (b) $p=0.09$, respectively. The solid line is the fitting result with the formula, $\sigma_2/\sigma_2(5K) = (1 - Be^{-c_2 \cdot T_c/T})$. (c)-(d) Plot of $\sigma_2/\sigma_2(5K)$ versus T_c/T for the Ca-YBCO microstrip line resonator with (c) $p=0.217$ and (d) $p=0.078$, respectively. The solid line is the fitting result with the formula, $\sigma_2/\sigma_2(5K) = (1 - Be^{-c_2 \cdot T_c/T})$178

Fig. 4.54. The doping dependence of the characteristic energy scale $E_{g_2}(0)$ and T_c of the YBCO and Ca-YBCO thin films was obtained from the fitting of σ_2179

Fig. 4.55. (a) The doping dependence of the characteristic energy scale $T_{\sigma_2}^*$ and T_c of the YBCO and Ca-YBCO thin films extracted from the microwave conductivity, $\sigma_2(T)$, measurements. (b) The doping dependence of the characteristic energy scale T_{θ}^{\max} , T_c , and T^{MF} sketched by Emery and Kivelson [88]. From (a) and (b), the same systematic tendency for $T_{\sigma_2}^*$ and T_{θ}^{\max} in the underdoped regime was shown. However, in the overdoped regime, $T_{\sigma_2}^*$ corresponds to the T^{MF}180

Fig. 4.56. The doping dependence of the factor, γ , extracted from the imaginary part conductivity, $\sigma_2(T)$, measurements for the YBCO and Ca-YBCO thin films.181

List of Tables

Chapter 2

Table 2.1. The experimental parameters of oxygen-content controlling for $Y_{0.7}Ca_{0.3}Ba_2Cu_3O_{7-\delta}$ and $YBa_2Cu_3O_{7-\delta}$ thin films which have been placed together in the same experimental condition were listed.	26
--	----

Chapter 4

Table 4.1. The penetration depth $\lambda(5K)$ and the energy gap $2\Delta_0/k_B T_c$ for the YBCO and Ca-YBCO films are obtained from microstrip ring resonator measurements.	94
Table 4.2. The penetration depth $\lambda(5K)$ and the energy gap $2\Delta_0/k_B T_c$ for the YBCO and Ca-YBCO thin films are obtained from microstrip line resonator measurements.	95
Table 4.3. Some parameters for the YBCO and Ca-YBCO thin films are obtained from the microwave and the resistivity measurements.	100
Table 4.4. The Fermi-liquid correction factor α^2 for the YBCO and Ca-YBCO thin films are obtained from the microwave ring resonators.	107
Table 4.5. The Fermi-liquid correction factor α^2 for the YBCO and Ca-YBCO thin films are obtained from the microstrip line resonators.	108
Table 4.6. Some parameters for the YBCO and Ca-YBCO ring resonators are obtained from the numerical fitting of the real-part conductivity σ_1	114
Table 4.7. Some parameters for the YBCO and Ca-YBCO microstrip line resonators are obtained from the numerical fitting of the real-part conductivity σ_1	118
Table 4.8. Some parameters for YBCO and Ca-YBCO ring resonators are obtained from the numerical fitting of the imaginary-part conductivity σ_2	124

Table 4.9. Some parameters for the YBCO and Ca-YBCO microstrip line resonators are obtained from the numerical fitting of the imaginary-part conductivity σ_2125

